Autonomous filling of creep cavities in Fe-Au alloys studied by synchrotron X-ray nano-tomography

Fang, H.; Versteylen, C. D.; Zhang, S.; Yang, Y.; Cloetens, P.; Ngan-Tillard, D.; Brück, E.; van der Zwaag, S.; van Dijk, N. H.

DOI
10.1016/j.actamat.2016.09.023

Publication date
2016

Document Version
Accepted author manuscript

Published in
Acta Materialia

Autonomous filling of creep cavities in Fe-Au alloys studied by synchrotron X-ray nano-tomography

H. Fang [a, b, *], C.D. Versteylen [a], S. Zhang [a], Y. Yang[c], P. Cloetens[c], D. Ngan-Tillard[d], E. Brück[a], S. van der Zwaag[b], N.H. van Dijk[a]

[a] Fundamental Aspects of Materials and Energy group, Faculty of Applied Sciences, Delft University of Technology, Mekelweg 15, 2629 JB Delft, The Netherlands.
[b] Novel Aerospace Materials group, Faculty of Aerospace Engineering, Delft University of Technology, Kluyverweg 1, 2629 HS, Delft, The Netherlands.
[c] European Synchrotron Radiation Facility, 38043 Grenoble Cedex 9, France.
[d] Department of Geoscience & Engineering, Faculty of Civil Engineering and Geosciences, Stevinweg 1, 2628 CN, Delft, The Netherlands.

A B S T R A C T

The autonomous filling of creep-loading induced grain-boundary cavities by gold-rich precipitates at a temperature of 550 ^{o}C has been studied as a function of the applied load for Fe-Au alloys using synchrotron X-ray nano-tomography. The alloy serves as a model alloy for future self-healing creep resistant steels. The size, shape and spatial distribution of cavities and precipitates are analyzed quantitatively in 3D at a nanometer resolution scale. The filling ratios for individual cavities are determined and thus a map of the filling ratio evolution is obtained. It is found that the gold-rich precipitates only form at cavity surfaces and thereby repair the creep cavity. The shape of the cavities changes from equiaxed to planar crack like morphologies as the cavities grow. The time evolution of the filling ratio is explained by a simple model considering isolated cavities as well as linked cavities. The model predictions are in good agreement with the measurements.

Keywords: Self healing, Creep, Fe alloys, Synchrotron radiation, X-ray tomography.

[*] **Corresponding author**. Fundamental Aspects of Materials and Energy Group, Faculty of Applied Sciences, Delft University of Technology, Mekelweg 15, 2629 JB, Delft, the Netherlands. *E-mail address*: H.Fang@tudelft.nl (H. Fang).

1. Introduction

Creep damage in steels occurs during long-term use at high temperatures and arises from the nucleation, growth and coalescence of grain-boundary cavities, which ultimately leads to catastrophic failure of the entire structure [1-2]. To date, most strategies [3-6] have aimed to tune the composition and microstructures of creep-resistant steels in such a way that the formation of creep damage is postponed, if not avoided. In the last two decades an alternative strategy has been explored to extend the lifetime of materials and structures via their ability to self-heal the early damage by the material themselves [7]. By now, this approach has been demonstrated to significantly enhance the component lifetime for a wide range of materials, including polymers, concrete, composite materials, aluminum alloys and steels [8-10].

Restricting the development of self healing materials to that of self healing metals, Laha and coworkers [11-13] observed a significant increase in creep lifetime in Cu and B enriched austenitic stainless steels, which was attributed to the healing of creep damage due to dynamic precipitation of either Cu or BN at the creep cavity surface. However, in more recent studies [14-15] on Fe-Cu and Fe-Cu-B-N model alloys, it was found that Cu precipitates do not only form in the grain boundaries, but to a larger extent also throughout the matrix. In order to enhance the defect-induced precipitation, while suppressing the undesired precipitation in the matrix at the same time, a high nucleation energy barrier for precipitation in the matrix and a strong driving force for segregation to cavity surface is required. Previous studies [16-17] showed that Au atoms in Fe-Au alloys have a strong preference to segregate and combine with Fe atoms to form Au-rich precipitates. This makes Au an excellent healing agent for the creep damage in ferrous alloys. Fe-Au alloys are therefore an ideal model system to study the self healing of creep damage. A detailed understanding will provide essential input to design future self-healing creep resistant steels. Extensive research [18-19] has been carried out subsequently to investigate the autonomous repair mechanism of the Fe-Au alloys during creep. Scanning electron microscopy (SEM) and X-ray photoelectron spectroscopy (XPS) observations confirmed the strong tendency of Au atoms to segregate on a free surface. Transmission electron microscopy (TEM) and small-angle neutron scattering (SANS) identified that the gold precipitation was induced and accelerated by the defects in the Fe-Au alloys. Electron probe micro-analysis (EPMA) and atom probe tomography (APT) quantified the local chemical compositions and thus indicated the diffusion pathways of Au atoms. However, all these measurements were limited to characterization of two-dimensional (2D) cross sections or a small three-dimensional (3D) region with a length size of several nanometers. In order to build a more comprehensive understanding of the repair mechanism of creep damage in Fe-Au alloys, the 3D microstructure needs to be resolved and studied at both nanometer and micrometer length scales.

Synchrotron X-ray tomography has developed into a powerful 3D imaging technique for non-invasive characterization of materials [20,21]. The high penetration power, high spatial resolution, as well as the multiple–contrast mechanisms make it an appealing method for the study of internal structures in metals. It has been employed

for investigating the size and shape of phases in metals such as aluminum alloys [22-24] and steels [25-26].

In the present study, synchrotron X-ray holotomography with a voxel size down to 25 nm was successfully employed to resolve the 3D structure of un-healed and healed creep damage in an Fe-Au (1 at.% Au) alloy. We determined and analyzed the size, shape and spatial distribution of the cavities and precipitates in creep-failed samples submitted to creep at various constant loads and a fixed temperature of 550 ^{o}C. From this we derived a model for the creep cavity filling and obtained a better insight in the mechanisms responsible for the formation and healing of creep cavities.

2. Materials and methods

2.1 Sample preparation and creep tests

The chemical composition of the Fe-Au alloy studied is listed in Table 1. The rolled sheet material was produced by Goodfellow. Miniature tensile test samples with a conventional dog-bone shape (a gauge length of 12.5 mm, a width of 6 mm and a thickness of 0.5 mm) were machined by spark erosion. These samples were then annealed at 868 ^{o}C for 5 h in an evacuated and sealed quartz tube filled with 200 mbar ultra-high purity argon and quenched in water. Subsequently, creep tests were carried out in vacuum on the as-quenched samples at a temperature of 550 ^{o}C and constant loads corresponding to initial stress levels of 60, 80, 100 and 117 MPa [18-19]. Bar-shaped samples with a square cross section of 200×200 μm^2 and a length of around 6 mm were cut by spark erosion from the uniform gauge section of the creep-failed samples for tomography experiments. The long axis of the bar-shaped samples was aligned with the stress axis in the creep experiments. The sample was taken such that the region to be characterized was between 2 and 4 mm away from the fracture surface. In addition to the X-ray tomography, the 2D microstructure of the samples was analyzed by a scanning electron microscope (JEOL JSM 6500F) equipped with an Autrata back-scattered electron detector. A detailed 2D characterization of the microstructure of these samples by electron microscopy and atom-probe tomography has been reported previously [18-19].

Table 1
The chemical composition of the Fe-Au alloy sample (wt.%).

Au	B	N	C	Ce	Fe
2.87	< 0.01	0.0085	0.0008	0.015	balanced

2.2 Synchrotron X-ray nano-tomography

For the morphological study of both the nano and micro-scale structures in the Fe-Au alloys, synchrotron hard X-ray tomography based on phase contrast with high spatial resolution was adopted. Holotomography measurements of the samples were conducted at the ID16A-NI nano-imaging beamline of the European Synchrotron Radiation Facility (ESRF) in Grenoble, France [27]. This new beamline offers a unique combination of nanofocus (≈ 20nm) and a very high photon flux (up to 10^{12} photons/s at $\Delta E/E \approx 1\%$). Two pairs of multilayer coated Kirkpatrick-Baez (KB) optics are used to focus the X-rays at 17 and 33.6 keV, respectively. The higher energy

of 33.6 keV was chosen in this experiment to optimize the transmission through the samples. Besides the benefits of the ability to perform nano-tomography with a high energy, the magnifying geometry of the cone beam also allows the switch between a large field of view (FOV) with 100 nm voxel size, and a finer FOV at a voxel size of 25 nm.

Due to the free space propagation of the X-ray beam the contrast in the images is dominated by phase contrast, related to the real part of the complex refractive index, which is determined by the electron density of the material. By measuring the Fresnel diffraction patterns at different effective propagation distances, the phase maps of the sample can be retrieved via holographic reconstruction, the so called phase retrieval procedure [28] implemented using GNU Octave software.

As shown in Fig. 1, the bar-shaped sample was mounted on the rotation stage of the tomography setup. During the scan, it was placed downstream of the KB focus and magnified radiographs were recorded onto an X-ray detector using a FReLoN charged-coupled device (CCD) with a 2048×2048 binned pixels array. For one tomography scan, 1500 projections were acquired with an exposure time of 1.00 s for a resolution of 100 nm and 1.25 s for the higher resolutions of 25 and 50 nm. Tomographies at four different focus-to-sample distances were acquired to complete one holotomography scan, which were subsequently used for phase retrieval. The 2D phase maps retrieved from the angular projections were then used as input for a tomographic reconstruction based on the filtered back projection (FBP) algorithm method (ESRF PyHST software package) [29]. The reconstructed 3D volumes were visualized and rendered with 3D visualization software Avizo 8.1 (FEI).

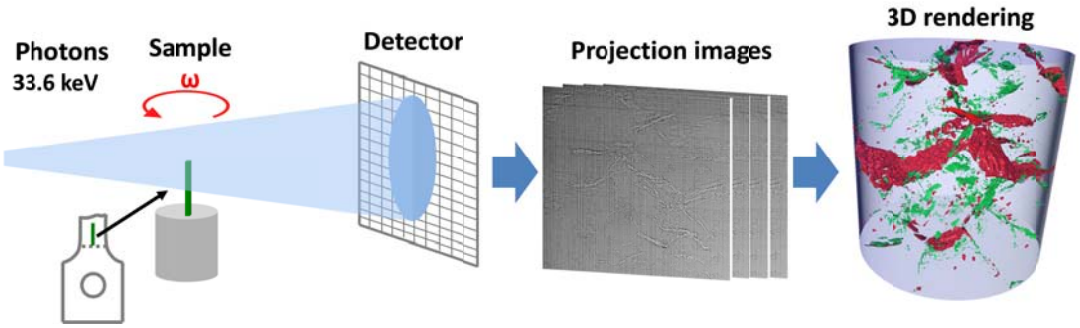

Fig. 1. Schematic diagram of the synchrotron X-ray holotomography imaging process. In the 3D rendering the precipitates and cavities are labelled in green and red, respectively, while the iron matrix is in transparent light grey.

The phases present in the creep-failed samples have previously been characterized as: (i) the Fe-Au alloy matrix (with a *bcc* structure), (ii) empty creep cavities and (iii) Au-rich precipitates (containing 80 at.% Au and 20 at.% Fe) [19]. In the present study, only the creep cavities and gold precipitates are of interest because they directly affect the self-healing of creep damage by site-selective precipitation of Au-rich precipitates at the creep cavity surface. Since the electron density of Au is much higher than that of Fe and that of vacuum is much smaller than that of Fe, the contrast difference between an empty cavity and an Au-rich precipitate is very large. Hence we

can clearly recognize the Au-rich precipitates as dark features and creep cavities as bright features. Both the precipitates and the creep cavities can be segmented by applying a threshold value for the local density variations (grey scale) in the 3D image. It should be noted that the quality of the segmentation strongly depends on the threshold value. The value was extensively tested to achieve an optimal contrast for the precipitates and the creep cavities. The segmentation provided binary images of the precipitate and the creep cavities for further analysis. In order to study the filling mechanism of the creep cavities in more detail we not only identified cavities and gold precipitates, but also determined the degree of pore filling by examining the co-location of pores and precipitates.

2.3 Data analysis

A quantitative analysis of both the creep cavities and the Au-rich precipitates, identified in the binary images, was performed using a MATLAB program with the DIPimage toolbox [30]. The shape of the objects can be characterized by several parameters. The shape complexity Ω_d (where d is the dimensionality of the object) is a dimensionless parameter in which the surface area of the object A is normalized by the surface area of a sphere with the same volume as the object V [31]. This parameter quantifies the irregularity of the shape. For three-dimensional objects (d = 3), the complexity corresponds to:

$$\Omega_3 \equiv \frac{A}{\pi^{1/3}(6V)^{2/3}} \tag{1}$$

The value of the shape complexity varies between $\Omega_3 = 1$ for a sphere and $\Omega_3 \to \infty$ for objects with a finite area A and a negligible volume ($V \to 0$). The reciprocal value of the three-dimensional shape complexity is also known as the sphericity $\Psi = 1/\Omega_3$ (where $0 \le \Psi \le 1$) [32].

An additional shape characterization is obtained by approximating the shape of the object by an equivalent ellipsoid with the same moment of inertia as the real object [33]. Assuming the composition of the particle to be uniform, the semi-axes of the ellipsoid a_j can be determined from the eigenvalues of I_j of the moment of inertia tensor $\mathbf{I}$:

$$a_j = \sqrt{\frac{5\left(Tr\left(\mathbf{I}\right) - 2I_j\right)}{2V}}, \quad j = 1, 2, 3 \tag{2}$$

where $Tr\,(\mathbf{I}) = I_{11} + I_{22} + I_{33}$ is the sum of the elements along the main diagonal of the moment of inertia tensor $\mathbf{I}$. The corresponding eigenvectors $\mathbf{B}_j$ representing the spatial orientation of the semi-axes can be calculated by solving $(\mathbf{I} - a_j\mathbf{1})\mathbf{B}_j = \mathbf{0}$, where $\mathbf{1}$ is the unit matrix. In the present work the major, intermediate and minor semi-axes (a_j) are expressed as a, b and c, respectively. Using these parameters the elongation E and flatness F are defined as [34]:

$$E = \frac{2a}{b + c} \tag{3}$$

$$F = \frac{b}{c} \tag{4}$$

For a sphere all axes are equal ($a = b = c$), resulting in an elongation of $E = 1$ and a flatness of $F = 1$. For a rod-shaped ellipsoid of revolution ($b = c$) with one long axis (a) one finds $E = a/c$ and $F = 1$, while for a sheet-shaped ellipsoid of revolution ($a = b$) with one short axis (c) one finds $E = 2a/(a + c)$ and $F = a/c$ (and thus $E = 2F/(F+1)$).

It is found that the combination of the complexity Ω_3, the elongation E and the flatness F provides an unambiguous quantitative approach to monitor the morphologic evolution of both the creep cavities and the precipitates. Based on these three combined descriptors the shape of both the cavities and the precipitates are classified as: (1) spheres, (2) equiaxed shapes, (3) rods, (4) sheets and (5) complex objects.

In order to determine the filling ratio of the creep cavities (*i.e.* the volume of connected Au precipitation over the volume of the original creep cavity) it is necessary to check for each open cavity how many precipitates are in direct contact with it and to determine the location of outer boundary of the pore-precipitate ensemble with the Fe-rich matrix. This was performed by dilating the particles by a predefined number of pixels in orthogonal directions and identifying the intersection. In this way, for each cavity the filling ratio (FR) by precipitation can be calculated:

$$FR = \frac{V_{precipitate}}{V_{cavity} + V_{precipitate}} \tag{5}$$

where $V_{precipitate}$ is the total volume of precipitates in contact with the cavity and V_{cavity} is the volume of the open cavity.

3. Results

3.1 Creep behavior and electron microscopy

The strain-time curves of the Fe-Au samples under different loads are shown in Fig. 2a and the derived stress dependent steady-state strain rate and rupture time are given in Fig. 2b and Fig. 2c, respectively [18-19]. All creep curves show the usual rapid strain increase in the initial stage (stage I) followed by a stage with an approximately constant strain rate (stage II) before the strain accelerated in the failure regime (stage III). The creep failure strain is about 0.10 for all samples. The creep lifetime is mainly controlled by the steady-state strain rate $\dot{\varepsilon}_{SS}$ in the secondary stage. It is found that $\dot{\varepsilon}_{SS}$ depends on the applied stress and fulfills a Sherby-Dorn relationship [35] with $\dot{\varepsilon}_{SS} \propto \sigma^{1.64}$ in the low stress region (≤ 100 MPa), while at a higher stress the stress exponent increases. This low stress exponent suggests the creep deformation is controlled by the combination of diffusion and dislocation motion [36]. The stress exponent for the lifetime is derived to be about -2 and becomes more negative at the highest stress. The change in the stress exponent of both the steady-state strain rate and the lifetime for a stress above 100 MPa suggests that there is a different creep mechanism at higher stresses.

Fig. 3 shows back-scattered SEM images of 2D cross-sections for the Fe-Au alloy

samples after creep at a temperature of 550 °C and a stress of 100 and 117 MPa, respectively. White features are gold precipitates and black features are creep cavities. It can be seen in Fig. 3a and 3b that the gold precipitates are formed inside the grain-boundary cavities and have an irregular shape that matches the morphology of the creep cavities. Fully filled cavities are observed along inclined grain boundaries, as shown in Fig. 3a. Partially filled cavities along grain boundaries that are oriented perpendicular to the applied stress are found in both Fig. 3a and 3b. Fig. 3b also shows an unfilled cavity at a grain-boundary junction. Gold depletion zones are indicated by darker regions in Fig. 3 and form close to the grain boundaries where gold precipitates have formed. More details of the 2D characterization of the microstructure can be found in [18-19]. As these observations are limited to 2D images it is difficult to establish how the cavity is filled by gold precipitation.

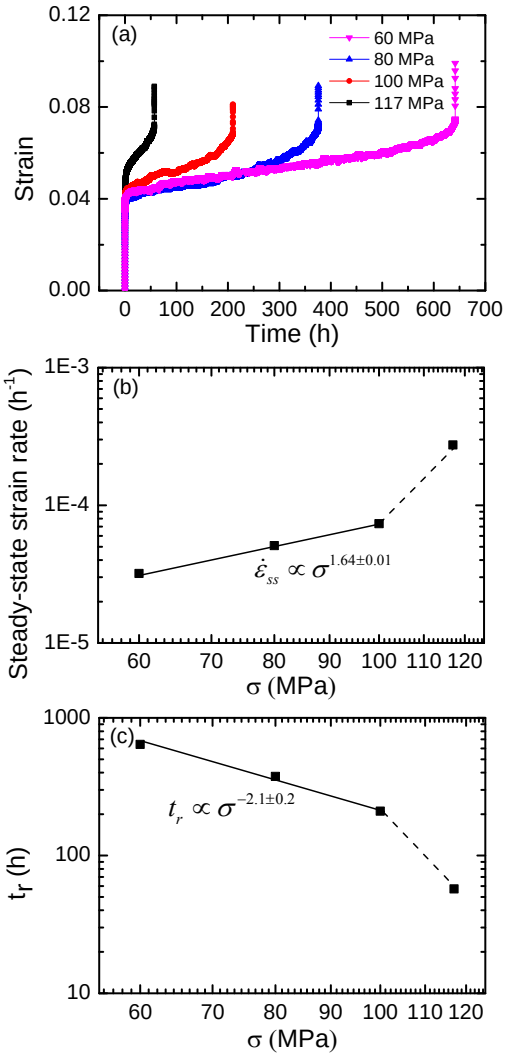

Fig. 2. (a) Creep curves of the Fe-Au samples creep loaded at 550 °C and 60, 80, 100 and 117 MPa and the derived stress dependence of (b) the steady-state strain rate and (c) the rupture time [18-19].

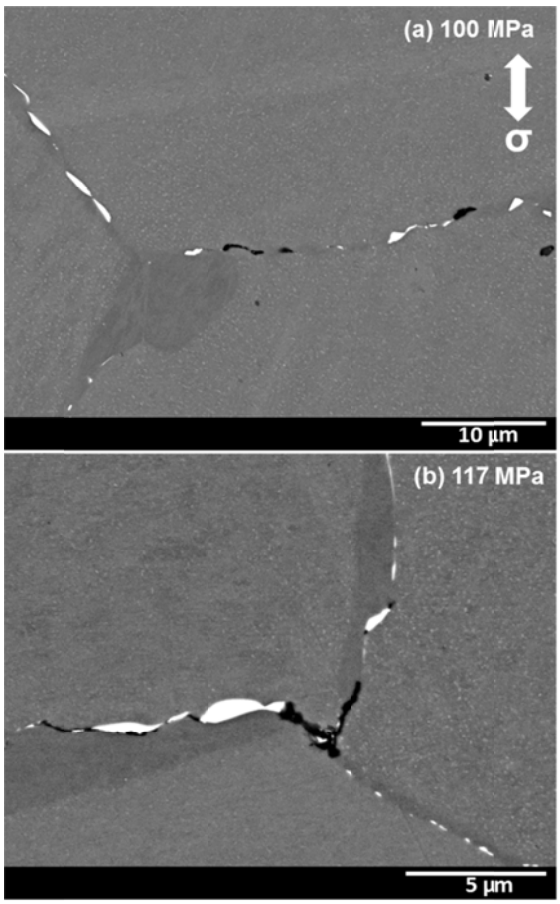

Fig. 3. Back-scattered scanning electron microscopy images of the Fe-Au alloy after creep at a temperature of 550 °C and a stress of (a) 100 MPa and (b) 117 MPa. Note that the white features are gold precipitates and the black features are creep cavities. The direction of the applied stress is indicated in (a).

3.2 Tomographic rendering

Fig. 4 shows the 3D tomographic renderings with a voxel size of 100 nm for the four creep-loaded samples. For these lower resolution imaging settings, the minimum size of identified cavities and precipitates is 0.3 µm (3 times the 100 nm voxel size). Objects with a smaller size are regarded as noise and ignored. It is shown in Fig. 4 that the spatial distribution of cavities and precipitates is heterogeneous. Most of the cavities are close to precipitates except for some small ones. The precipitates range from small isolated spherical or equiaxed particles to large coalesced objects with complicated shapes that follow the profile of the cavities. The big cavities are approximately oriented perpendicular to the stress direction. As the field of view (FOV) is around 200 µm high with a transverse cross section of 200×200 μm^2, the probed 3D volume contains about 60 grains for an average grain size of 57 µm. This indicates that the dataset with a voxel size of 100 nm provides meaningful quantitative statistics.

Of particular interest are also the details of large transverse grain boundary cavities shown in Fig. 5 recorded with the smaller voxel of 25 nm. At the lower loads, i.e. for the longer failure times, the grain boundary cavity has enough time to grow

and ultimately covers an entire grain-boundary facet. The figure also shows that parts of the grain-boundary cavity surfaces are covered by precipitates. As the smallest characterized particle size is 75 nm (3 times the 25 nm voxel size), we can probe the early growth stage of the cavities and the centers of these small particles could be regarded as nucleation sites. The average spacing between the smallest cavities is estimated to be around 4 μm.

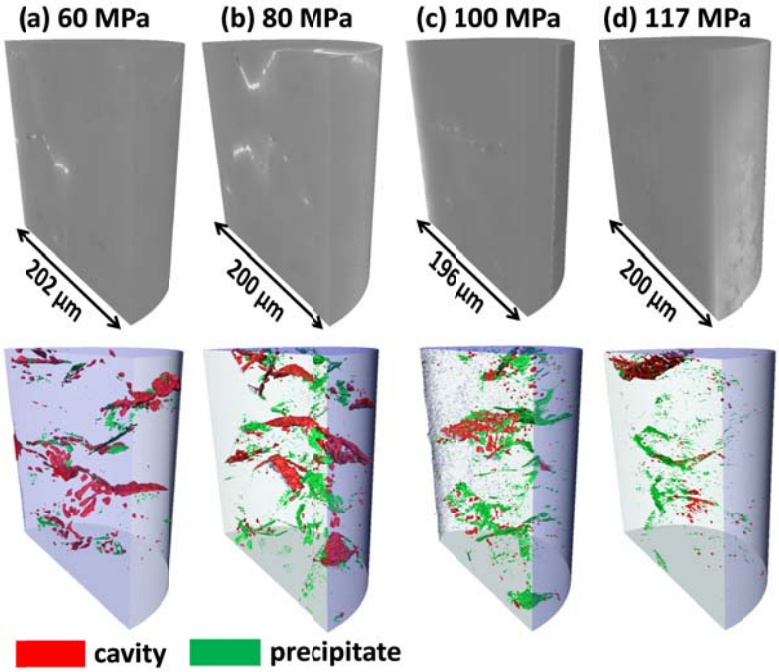

Fig. 4. Overview of the 3D tomographic renderings before (upper part) and after (bottom part) phase segmentation with a voxel size of 100 nm for samples after creep at a temperature of 550 ^{o}C and a load of (a) 60 MPa, (b) 80 MPa, (c) 100 MPa and (d) 117 MPa. The applied stress is along the vertical direction.

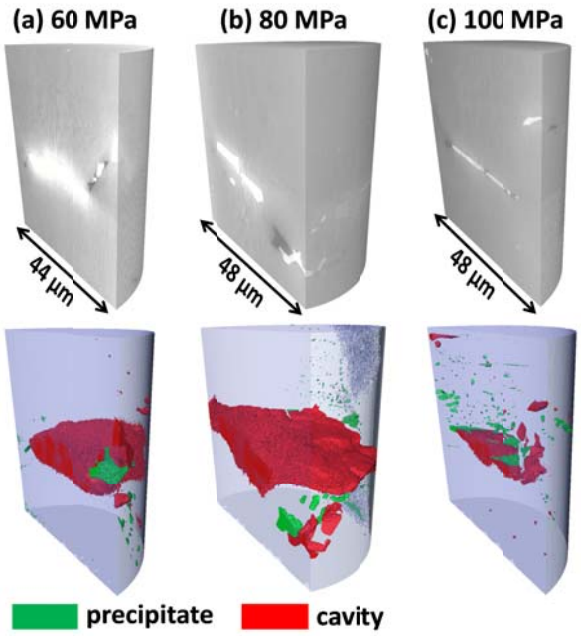

Fig. 5. Overview of the 3D tomographic renderings before (upper part) and after (bottom part) phase segmentation with a voxel size of 25 nm for samples after creep at a temperature of 550 ^{o}C and a load of (a) 60 MPa, (b) 80 MPa and (c) 100 MPa. The applied stress is along the vertical direction.

To better understand the spatial distribution of the cavities and precipitates, the region of interest (ROI) shown in Fig. 6 is extracted from the creep-failed sample at 80 MPa and 550 ^{o}C (see in the Supplementary Material Fig. S1-S3 for the results at a stress of 60, 100 and 117 MPa and movie S4 for a 3D angular view on the results for a stress of 80 MPa). By projecting this microstructure from different angles, it is found that the positions of the precipitates clearly delineate the grain boundaries as shown best in the top view. This is in agreement with the previous SEM studies which showed that the precipitates in the Fe-Au alloy are formed exclusively at grain boundaries and at pre-formed cavities [18-19]. With the grain boundary positions identified, it is found that most of cavities are indeed located on the grain boundaries, while some small cavities appear in the matrix. This suggests that not all cavities nucleate on the grain boundary. However, only the grain boundary cavities are able to grow into larger sizes. Fig. 6 also reveals that the particles formed at different locations have different shapes: particles dispersively distributed on the grain boundaries and within the matrix are mainly spherical or equiaxed; particles on the inclined grain boundaries are more elongated or flattened, while particles located on the grain junctions have a relatively complicated shape.

Supplementary video related to this article can be found at http://dx.doi.org/10.1016/j.actamat.2016.09.023.

3.3 Shape classification of cavities and precipitates

In order to understand the fine details of the healing reaction and the interaction between damage formation and cavity filling, the particles morphologies as

determined by tomography are based on their elongation (E), flatness (F) and complexity values (Ω_3) classified in 5 categories: (a) spherical, (b) equiaxed, (c) rods, (d) sheets and (e) complex shapes. The criteria for the classifications are listed in Table 2. In Fig. 7 examples are shown for the classified cavity and precipitate shapes (with their particle volume).

Table 2
Classifications of different shapes based on the Elongation (E), Flatness (F) and Complexity (Ω_3) of the objects.

	E	F	Ω_3
Sphere	-	-	$\Omega_3 \leq 1.15$
Equiaxed	< 5	< 5	$1.15 < \Omega_3 < 2.5$
Rod	≥ 5	< 5	$1.15 < \Omega_3 < 2.5$
Sheet	-	≥ 5	$1.15 < \Omega_3 < 2.5$
Complex	-	-	$\Omega_3 \geq 2.5$

Fig. 8a and 8b respectively show the flatness versus the elongation and the complexity as a function of the volume for over 8000 individual precipitates in the sample loaded at 80 MPa. In Fig. 8a the spherical particles occupy the left bottom corner, as they are characterized by $F \approx E \approx 1$. Next are the equiaxed particles which show slightly higher, yet comparable values of E and F. The rod-like particles are more elongated, while the sheet particles are more flattened. Therefore, the rod-like particles are located in the right bottom region while the sheet-like particles are located in the top region in Fig. 8a. The complex particles are distinguished by their complexity (Ω_3) and as can be seen in Fig. 8a they may have a more randomly relationship between E and F. In Fig. 8b the spherical particles with the lowest Ω_3 have small volumes, the complex ones have large volumes, while the equiaxed, rod and sheet types fall in between. For the precipitate population of other samples, a similar behavior was observed. This demonstrates that the proposed classification is a reliable way to identify different types of particles.

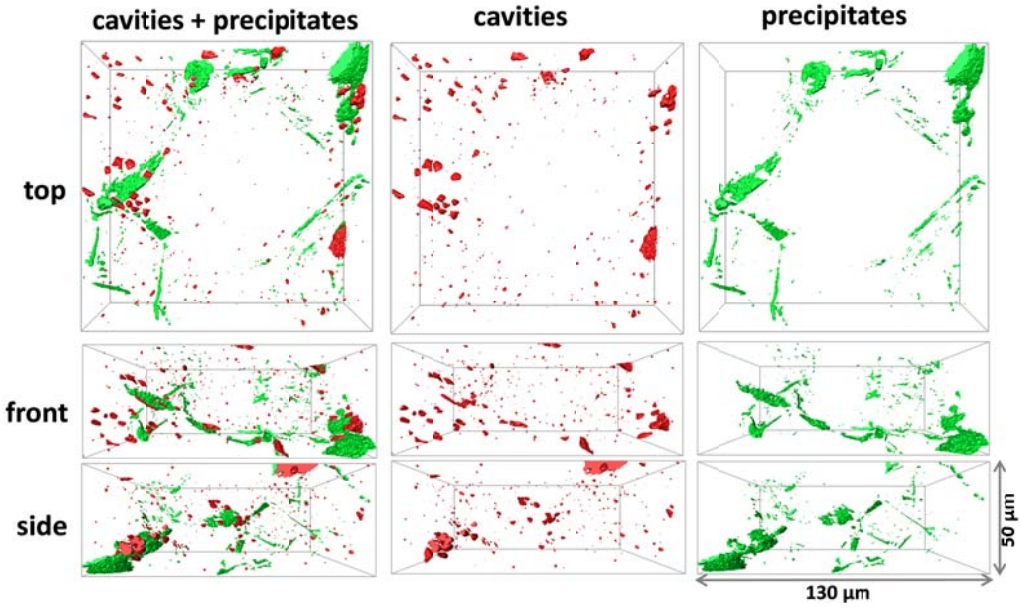

Fig. 6. A ROI with a size of 130×130×50 µm^3 revealing the microstructure of the Fe-Au alloy after creep failure at 550 ^{o}C and 80 MPa. The applied stress is normal to the top view.

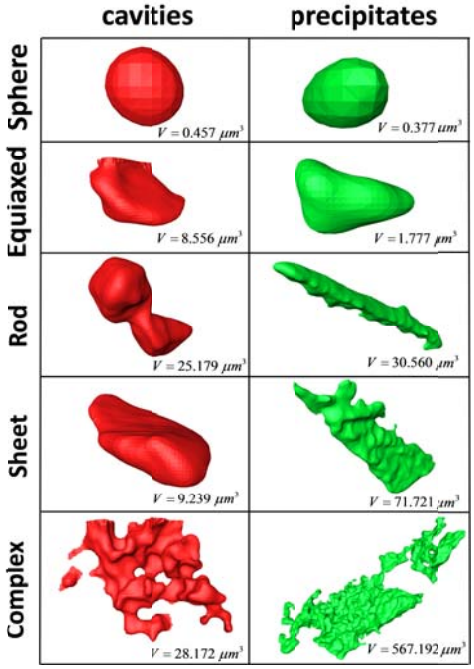

Fig. 7. Examples of classified cavity and precipitate shapes for the Fe-Au alloy after creep at 550 ^{o}C and 80 MPa (top view projections extracted from Fig. 6). The particle volumes are also indicated.

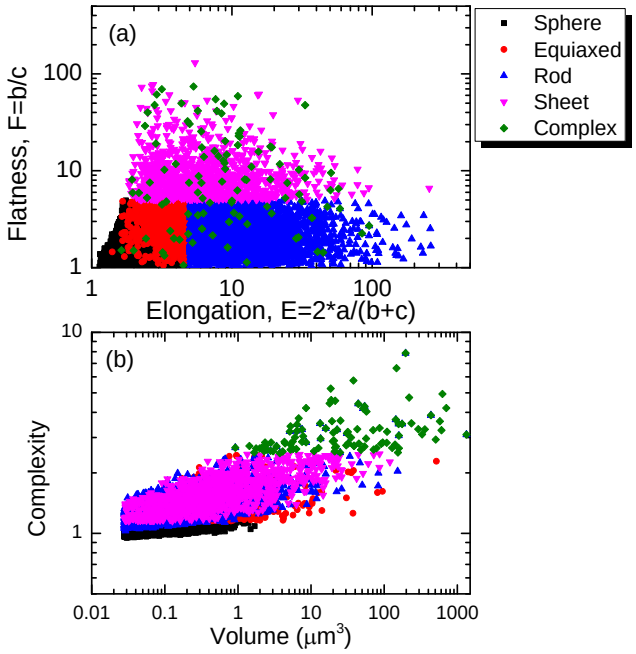

Fig. 8. (a) Flatness F as a function of the elongation E and (b) the complexity as a function of the particle volume for 8139 precipitates identified from the probed volume of the Fe-Au alloy after creep at 550 °C and 80 MPa.

3.4 Size distribution

Fig. 9a and 9b show the number distribution D_N versus the equivalent diameter for the cavities and the precipitates, respectively. The corresponding volume distributions D_V are shown in Fig. 9c and 9d. The equivalent particle diameter (EqDiameter) d is the diameter of a sphere with the same volume as the particle. As shown in Fig. 9a and 9b, the number distribution of the cavities and precipitates can be fitted to a log-normal distribution:

$$D_N(d) = \frac{N_0}{dw\sqrt{2\pi}} \exp\left(-\frac{\left\{\ln(d) - \ln(\bar{d})\right\}^2}{2w^2} \right) \tag{6}$$

where N_0 is the number density, $\bar{d}$ the mean value and w the relative distribution width of the equivalent diameter. The fitted values are listed in Table 3.

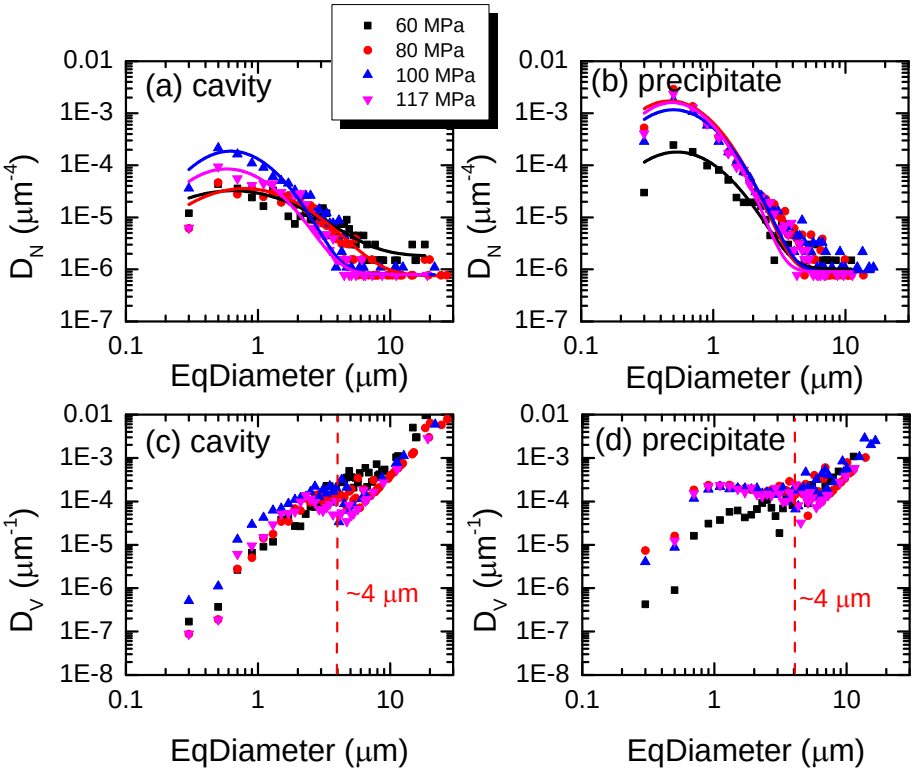

Fig. 9. Number distribution D_N of (a) cavities and (b) precipitates and the volume distribution D_V of (c) cavities and (d) precipitates as a function of the equivalent diameter d for the Fe-Au alloy after creep at 550 °C. The scatter data points are statistics of the tomographic result with a voxel size of 100 nm per voxel and the solid curves are the log-normal fittings.

Table 3

Fitted parameters N_0, $\bar{d}$ and w for the log-normal size distribution of cavities and precipitates after creep at an applied stress of σ = 60, 80, 100 and 117 MPa. In between brackets is the error in the last digit. The volume fraction f_V is obtained directly from the 3D tomographic volumes.

Phase	Σ (MPa)	N_0 (μm^{-3})	$\bar{d}$ (μm)	w	f_V (%)
Cavities	60	$7.0(5)\times10^{-5}$	1.5(1)	0.92(8)	0.64
	80	$7.6(3)\times10^{-5}$	1.50(6)	0.80(3)	0.76
	100	$1.94(6)\times10^{-4}$	0.86(2)	0.57(2)	0.24
	117	$9.2(5)\times10^{-5}$	0.85(4)	0.62(4)	0.11
Precipitates	60	$1.7(1)\times10^{-4}$	0.76(4)	0.60(5)	0.098
	80	$1.3(1)\times10^{-3}$	0.63(4)	0.54(6)	0.24
	100	$9.3(6)\times10^{-4}$	0.67(3)	0.55(4)	0.35
	117	$1.11(7)\times10^{-3}$	0.63(3)	0.50(4)	0.14

The fits indicate that the average diameter $\bar{d}$ of the cavities is about 1.50 μm

for the samples loaded at 60 and 80 MPa and about 0.85 μm for the samples loaded at 100 and 117 MPa. The width of the cavity size distribution increases with decreasing applied stress, as indicated by the *w* value reported in Table 3. As the average growth time is increased with increasing lifetime (*i.e.* decreasing applied stress), the coalescence of cavities is more enhanced at low stresses. The coarsening of the cavities in the later creep stages could occur by merging small cavities, which leads to both a decrease of the cavity number and an increase of the cavity size. In Table 3 it is indicated that the number density of cavities in the samples loaded at 60 and 80 MPa is smaller than at 100 and 117 MPa. For precipitates both $\bar{d}$ and *w* remain nearly constant, except for the sample loaded at 60 MPa, which has a slightly larger $\bar{d}$ value. This is mainly attributed to the fact that there are much fewer spherical precipitates in the sample loaded at 60 MPa compared to the other samples. As there are more coalesced cavities in the sample loaded at 60 MPa, the precipitates grow continuously at the large cavity surface with less chance to nucleate at small cavities, which leads to much less spherical precipitates and a greater value of $\bar{d}$.

The volume distributions D_V of both cavities and precipitates show two different regions with a cross-over around $d \approx 4$ μm, as shown in Fig. 9c and 9d. This value is similar to the average spacing between cavities derived from Fig.5. When $d < 4$ μm, the cavities and precipitates show a peak in D_V around 2.2 and 1.5 μm, respectively. In contrast, when $d > 4$ μm, the particles are more likely to have coalesced to form large volume objects, resulting in a continuous increase in D_V.

3.5 Filling ratio of the creep cavities

Fig. 10 shows the degree of filling for each creep cavity as a function of their volume for the four different applied stress levels. The obtained filling ratios (defined in Eq. 5) are presented with a subdivision into the identified shape types. Unfilled cavities correspond to $FR = 0$, completely filled cavities to $FR = 1$ and partially filled cavities to $0 < FR < 1$. The resolution limit for the volume in the determination of the filling ratio corresponds to 5 times the resolution ($V_{min} = (5 \times 0.1\mu m)^3 = 0.125\ \mu m^3$). Therefore, for all cavities or precipitates smaller than 0.1 μm^3 the filling ratio can only be 0 or 1.

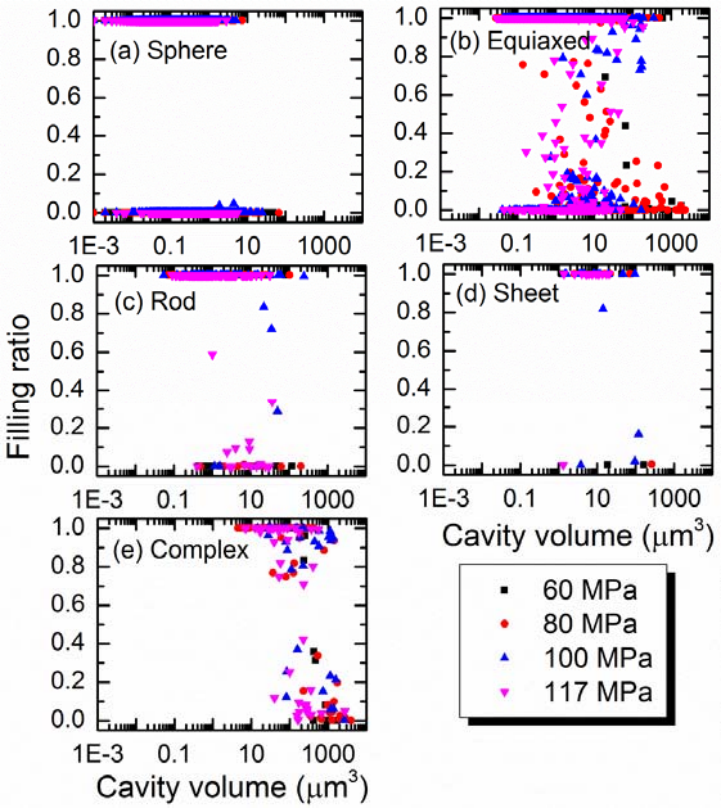

Fig. 10. Filling ratio of individual creep cavities as a function of the cavity volume in the Fe-Au alloy after creep at a temperature of 550 °C and a load of 60, 80, 100 and 117 MPa classified into: (a) spherical cavities, (b) equiaxed cavities, (c) rod-like shaped cavities, (d) sheet-shaped cavities and (e) complex cavities. The cavities were identified from the data obtained for a voxel size of 100 nm.

Fig. 10a shows that the spherical cavities (n = 1474) span the volume range of 10^{-3} to 100 μm^3, while the spherical precipitates (n = 9690) span the volume range 10^{-3} to 10 μm^3. This suggests that cavities form prior to the precipitates, which supports the viewpoint that the precipitates are induced by the cavities. Somewhat surprisingly, no partially filled spherical cavities were observed. In the case of equiaxed cavities (n = 591) and precipitates (n = 1779), the largest volume of such an (unfilled) cavity was 3000 μm^3, while that of the largest fully filled precipitate was 800 μm^3. Again, the largest cavity volume well exceeded the largest precipitate volume. Unlike the case of the well-defined spherical particles, in the case of equiaxed particles partial filling was frequently observed (n = 249) over the volume range of 0.1 to 100 μm^3. Partial filing was particularly obvious for the sample tested at the highest load level. Low level partial filling of the largest cavities was manifest for the sample loaded at a stress of 80 MPa.

In the case of rod-like cavities (n = 26) and precipitates (n = 336) (Fig. 10c), the maximum size of the cavities and that of the precipitates are about equal. Furthermore, the fraction of partially filled (large) cavities is very low. This suggests that rod like cavities remain empty for a relatively long time, but once the deposition process has been triggered the filling of the cavities proceeds rather quickly. A similar conclusion

can be drawn in the case of sheet like cavities (Fig. 10d), which occurred less frequently (n = 45). In this case most of the sheet structures are fully filled (n = 38), which is not surprising if the nucleation density of a gold-rich precipitate is surface area determined.

Finally, Fig. 10e shows the filling fractions for complex shaped cavities. The figure shows that such (relatively large) defects occur primarily at higher stress levels. At a nominal stress level of 80 MPa all such cavities are fully filled. At higher stress levels primarily partially filled structures are observed, which confirms the notion that the complex shaped structures reflect the merging of local damage sites just prior to catastrophic failure of the sample.

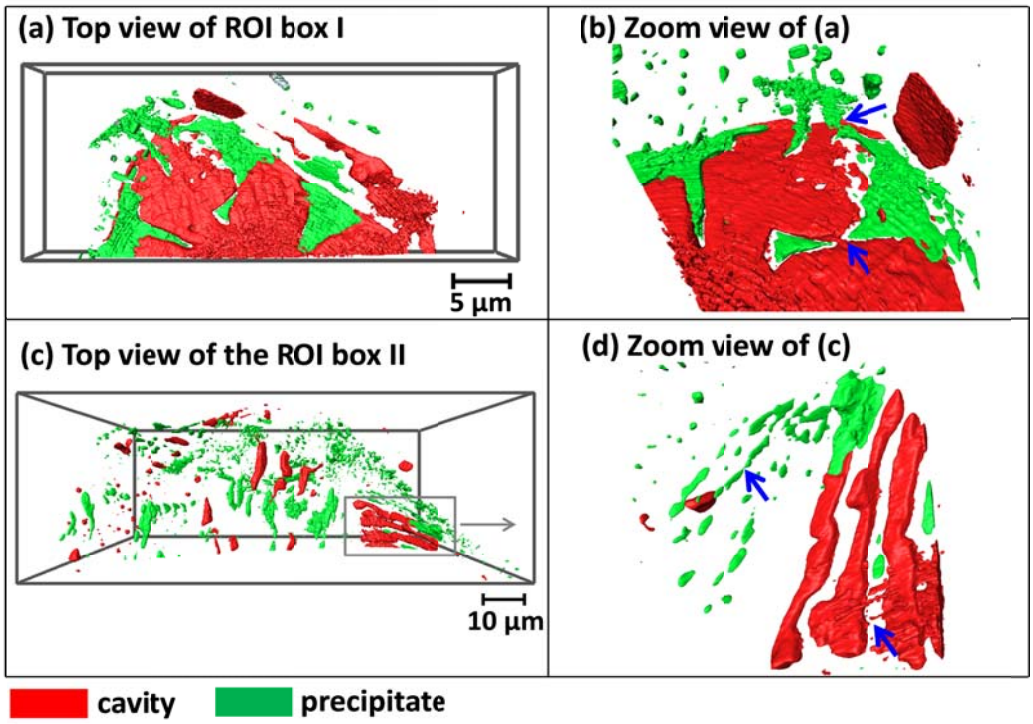

Fig. 11. Examples of creep cavities partially filled by precipitates. The ROI is extracted from the tomographic 3D rendering of the Fe-Au alloy after creep at a temperature of 550 ^{o}C and a load of (a, b) 100 MPa and (c, d) 117 MPa, respectively. The blue arrows in the figure show the linkage of cavities or precipitates.

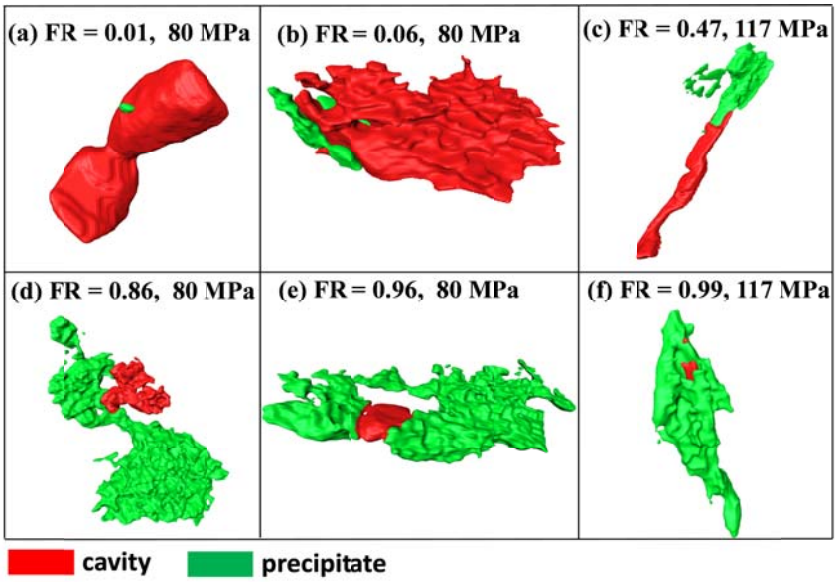

Fig. 12. Examples (top view) showing cavities with different filling ratios (*FR*). The applied stress is normal to the top view.

We will now focus in more detail on the filling of cavities at the grain boundaries. Fig. 11a and 11b show a big transverse grain boundary cavity partially filled by several precipitates. Due to the filling by precipitation at the cavity surface, this cavity cannot develop to cover the whole transverse grain boundary. Instead this cavity extends into the locations where less precipitates are formed and was linked up to generate a large cavity with a complex shape. This suggests that the precipitation could impede the growth of the large cavity although the linkage of the cavity is unstoppable. Smaller grain-boundary cavities are shown in Fig. 11c and 11d. A nearly identical spacing of about 4 μm is observed between the small cavities (unfilled and filled) at the transverse grain boundary. As the cavities have not coalesced significantly in this stage, the precipitates are able to completely fill some of them. Fig. 11d shows three rod-like cavities formed at the inclined grain boundary with a spacing of about 2 μm between them. It is interesting to note that the orientations of the cavities are identical to the grain boundary sliding (GBS) direction, which suggests that GBS favors the elongation of the cavities. In the meantime the linkage between these cavities proceeds, which is indicated by the arrow in Fig. 11d. From this detailed observation we can conclude that the cavities nucleate with a certain spacing between them at either transverse or inclined grain boundaries. The precipitates can fill small cavities efficiently, whereas once the cavities link together to form large ones it is too late to fill them completely.

Fig. 12 shows several examples of partially filled creep cavities produced at different stress levels. The observed structures indicate that the filling process generally starts from one location and develops until the cavity is completely filled. The necking in Fig. 12a suggests that this rod type cavity, which is located on the inclined grain boundary with respect to the applied stress, is the result of the coalescence of two equiaxed cavities. The resulting topology results in a small *FR*

value for rod like structures. This situation is comparable to that of Fig. 12b, in which the linkage of neighbouring cavities results in a big open cavity, but a low value of *FR*. In contrast, when the precipitation is induced soon after the nucleation of the cavity the cavity filling by the precipitate can accommodate the growth of the cavity leading to the high *FR* values found for the cavities shown in Fig. 12d-f. Fig. 12c shows that a rod-like cavity is nearly half filled (*FR* = 0.47) by the precipitate from one side. It is interesting to note in Fig. 12f that the open cavity has been fully encapsulated. This further demonstrates that the precipitate is filling the cavity rather than inducing the formation of the cavity.

4. Discussion

4.1 Growth modes of the creep cavities

The development of a creep cavity consists of nucleation, growth and coalescence processes. As these processes can happen simultaneously over the whole creep lifetime, it is difficult to analyze each process separately. However, combining an analysis of the locations and the different types of cavities can provide an insight into the cavity evolution.

As the resolution limit (≈ 3 times the voxel size, *i.e.* 75 nm) is close to the predicted size of the critical nucleus of about 50 nm [37], the cavities with a size $d < 1$ μm illustrate the early growth stage and preferred nucleation sites of the cavities. The location of the creep cavities shown in the 3D tomographic renderings indicates that grain boundaries are the preferred positions for the nucleation of cavities. A cavity may nucleate on a transverse grain boundary by the accumulation of the vacancies, while a cavity at an inclined grain boundary or triple point (partially) may be the result of grain boundary sliding (GBS). Once a cavity has nucleated on the grain boundary, the subsequent growth involves the vacancies diffusion along the cavity surface (surface diffusion), followed by diffusion along the grain boundary (grain-boundary diffusion), which finally causes the grain displacement leading to matrix creep [38]. When the surface diffusion is rapid enough, the cavity is able to maintain its quasi-equilibrium shape, as shown in Fig. 13a. Normally this quasi-equilibrium shape is lens-shaped with an angle of $\psi \approx 75^{o}$ between the tangent to the cavity surface and the plane of the grain boundary. However, when the surface diffusion is not much faster than the grain-boundary diffusion, the cavity cannot attain the equilibrium shape and develops into a crack-like cavity [39]. A cavity located at an inclined grain boundary may be distorted and elongated due to GBS [40], as shown in Fig. 13b. In conclusion, the tomography data suggest that both the grain-boundary diffusion and GBS play a role in the cavity growth in the Fe-Au alloy samples.

Different growth mechanisms of creep cavities have been analyzed extensively inprevious studies [37-45]. Several parameters have been proposed to define the growth mode. The evolution of cavity shape depends on the diffusivity ratio Δ [39] defined as:

$$\Delta = \frac{D_s \delta_s}{D_{GB} \delta_{GB}} \tag{7}$$

where D_s and D_{GB} are the surface diffusivity and grain boundary diffusivity,

respectively. The diffusivity corresponds to $D = D_0\exp(-Q/RT)$ with a constant pre-factor D_0, an activation energy Q, the gas constant R and the absolute temperature T. The variables δ_s and δ_{GB} are the surface and grain-boundary diffusion thickness, respectively. The surface diffusion layer thickness is estimated by $\delta_s = \Omega^{1/3}$, where Ω is the volume per atom [39]. The grain boundary diffusion layer thickness is assumed to be two atomic layers ($\delta_{GB} \approx 2\delta_s \approx 5\times10^{-10}$ m) [46]. In the present work, a value for Δ of 1.3 was estimated based on the values reported in the literature [38]. This suggests the surface diffusion is comparable to the grain boundary diffusion. According to [39], the cavity growth takes place maintaining a quasi-equilibrium shape as long as

$$\sigma < 1.9\left(\frac{\gamma_s}{r}\right)\left(1+1.3\frac{\Delta\lambda}{r}\right) \tag{8}$$

and transfers into a crack-like shape when

$$\sigma > 3.5\left(\frac{\gamma_s}{r}\right)\left(1+1.2\frac{\Delta\lambda}{r}\right) \tag{9}$$

where σ is the applied stress, γ_s the interfacial energy, r the cavity radius and λ the cavity spacing (center-to-center distance between the cavities). Assuming γ_s = 1.95 J/m^2, Δ = 1.3 and λ = 4 μm, the cavity can attain the equilibrium shape when the cavity radius r is less than 0.68, 0.58, 0.52 and 0.48 μm at σ = 60, 80, 100 and 117 MPa, respectively. The cavity would develop into crack-like shape when r is larger than 0.90, 0.77, 0.69 and 0.63 μm at σ = 60, 80, 100 and 117 MPa, respectively. It is estimated that the shape of the cavity shows a transition when $0.48 < r < 0.90$ μm from the equilibrium shape to the crack-like shape as the cavity growth proceeds. This is reflected in the examples of Fig. 13.

To address the influence of the creep flow on the diffusive cavity growth, Needleman and Rice proposed to estimate the diffusion length Λ [38] from:

$$\Lambda = \left(\frac{D_{GB}\delta_{GB}\Omega\sigma}{kT\dot{\varepsilon}}\right)^{1/3} \tag{10}$$

where $\dot{\varepsilon}$ the strain rate, k Boltzmann's constant and T the absolute temperature. The diffusion length is calculated to be Λ = 2.60, 2.41, 2.36 and 1.65 μm for σ = 60, 80, 100 and 117 MPa, respectively. The value of Λ is comparable to half of the average cavity spacing λ and slightly increases with decreasing applied stress. This indicates that both diffusion and creep flow control the cavity growth. As the vacancies diffuse from the cavity surface to the tip and then along the grain boundary, matrix creep flow is allowed to occur, resulting in a deformation of the grains. This accommodates and favors the cavity growth by transporting vacancies over shorter distances. Therefore, it is suggested that the growth of the creep cavities in this Fe-Au alloy occurs in a coupled diffusion and creep-flow mode. The numerical description of this sort of creep behavior has been presented by Chen and Argon [47].

In Fig. 14 the relationship between the average volume of the creep cavities and precipitates is shown for two shape groups as a function of the rupture time. The

fitting curves indicate that the average volume has a power-law dependence on the rupture time, expressed as $V = k\, t^n$. The derived values of the pre-factor k and time exponent n are summarized in Table 4. As the creep cavity growth is controlled by both diffusion and creep flow (the strain rate that is related to the applied stress), the pre-factor for cavity growth k_{cav} is expected to be proportional to the applied stress σ and can be expressed as $k_{cav} = k_0(\sigma / \sigma_0)$ where k_0 is a temperature dependent constant at a reference stress σ_0 (σ_0 = 100 MPa in Table 4). It is shown that the time exponent for the growth of cavities with spherical and equiaxed shapes is similar to the value for the growth of precipitates. The time exponent of cavities in rod, sheet and complex shapes increases, while the time exponent of precipitates in these shapes remains the same. Based on the previous analysis of the cavity growth mechanism, it is postulated that the spherical and equiaxed shaped cavities correspond to the early growth stage before coalescence, while the rod, sheet and complex types are most likely formed by coalescence in the later growth stage. This suggests that the coalescence of cavities accelerates the cavity growth, resulting in an increase of the time exponent. In contrast, the growth of precipitates is mainly controlled by the bulk diffusion of gold, which is insensitive to the stress, and therefore its time exponent for growth does not change.

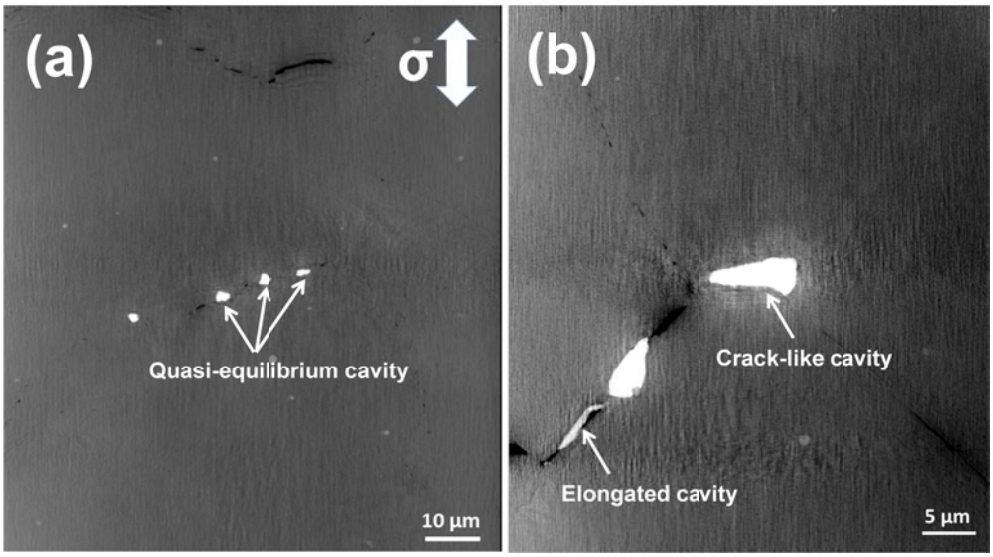

Fig. 13. Two tomography slices parallel to the applied stress show different growth modes of the creep cavities in the Fe-Au alloy sample after creep at (a) 117 MPa and (b) 60 MPa. Quasi-equilibrium cavities, crack-like cavities at a transverse grain boundary and an elongated cavity at an inclined grain boundary are indicated by the arrows.

4.2 Filling mechanism of the creep cavities

Previous studies [16-19] have shown that the gold precipitates can only form at defect sites due to the high energy barrier for their nucleation in the matrix. It is found that the Au atoms first segregate on the cavity surface and then form Au-rich precipitates (with about 20 at.% Fe at T = 550 °C). These observations are further clarified by the present tomography measurements that show a close correlation between the size, shape and spatial distribution of the cavities and precipitates. Furthermore, the degree of filling of each cavity has been deduced by this 3D nano-imaging technique, which allows a more detailed evaluation of the pore filling behavior.

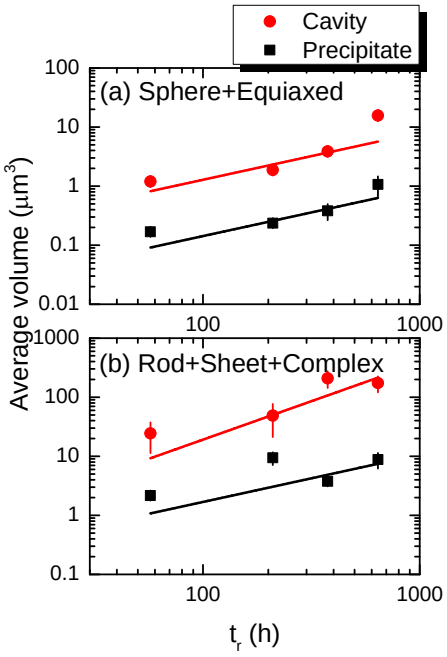

Fig. 14. Average volume of the precipitates and cavities grouped into (a) spherical and equiaxed shaped and (b) rod, sheet and complex shaped particles as a function of the rupture time.

Table 4

The derived parameters from a fit of the average volume V versus the rupture time t to a power law dependence of the form $V = k\, t^n$ for the creep cavities and precipitates subdivided into two different shape groups. For cavities the pre-factor k is assumed to be proportional to the applied stress. Listed is the value at a reference stress of σ = 100 MPa. For the precipitates the pre-factor k is independent of stress. In between brackets is the error in the last digit.

	Cavities		Precipitates	
Shape	k (100 MPa) (µm^{3}h$^{-0.8}$)	n	k (µm^{3}h$^{-0.8}$)	n
Sphere + Equiaxed	0.033(6)	0.8	0.0036(5)	0.8
Rod+Sheet+Complex	0.05(1)	1.3	0.04(1)	0.8

Essentially the self-healing kinetics is controlled by the relative rates of the damage (creep cavity) formation and healing (gold precipitation). Depending on the local conditions, the gold precipitation is triggered by the nucleation of creep cavities and becomes active when the cavities reach a characteristic size V_0. It is found in Fig. 10 that V_0 can vary between 0.1 and 100 μm^3. In order to evaluate the self-healing kinetics for a single cavity, we propose two different cases: (i) the cavity growth associated with the filling by the precipitates takes place without linkage with other cavities (coalescence); (ii) the growing cavity links with other cavities after it reaches a specific size V_1.

For the first case, it is assumed that the filling starts for a cavity volume V_0. After that, the cavity volume V_{cav} (including the filled and unfilled part) follows a power law with a constant time exponent m. Simultaneously, the gold atoms diffuse to the cavity surface and form a gold precipitate with a volume V_{prec} that follows a power law with a constant time exponent n:

$$V_{cav} = V_0 + k_{cav} t^m \tag{11}$$

$$V_{prec} = k_{prec} t^n \tag{12}$$

where k_{cav} and k_{prec} quantify the combined effects of stress and local conditions (*e.g.* the grain size and local grain-boundary orientation) on the growth of the creep cavity and precipitate, respectively. By taking the ratio of their volumes, the filling ratio FR is obtained:

$$FR = \frac{V_{prec}}{V_{cav}} = \frac{k_{prec}}{V_{cav}} \left(\frac{V_{cav} - V_0}{k_{cav}} \right)^{\frac{n}{m}} \tag{13}$$

Without linkage the time exponents m and n are expected to be equal as they are both diffusion controlled. This is in agreement with the parallel slopes for the time evolution of the average volume for spherical and equiaxed shaped objects, as shown in Fig. 14a and supported by previous studies [19,48-49]. Therefore, Eq. 13 can be simplified to:

$$FR = \frac{k_{prec}}{k_{cav}} \left(1 - \frac{V_0}{V_{cav}} \right) \tag{14}$$

where the filling ratio is purely controlled by the ratio k_{prec}/k_{cav} and the characteristic volume V_0. For $k_{prec} > k_{cav}$ complete filling (FR = 1) is achieved for $V_{cav} = V_0[k_{prec}/(k_{prec} - k_{cav})]$ at $t = [V_0/(k_{prec} - k_{cav})]^{1/m}$.

However, if the cavity links with other cavities then the self-healing kinetics would change. The cavity volume V_{cav} can in this case be described by an increase in the growth exponent of the cavity to $m+\Delta m > m$ after a critical time t_{link} when linkage starts to take place (or equivalently, beyond a critical volume $V_{cav} > V_1$ for $t > t_{link}$). For $t > t_{link}$ the cavity volume then corresponds to:

$$V_{cav} = V_1 + k_{cav,link} \left(t - t_{link} \right)^{m+\Delta m} \qquad (V_{cav} > V_1) \tag{15}$$

$$V_{prec} = k_{prec} t^n \tag{16}$$

with $V_1 = V_0 + k_{cav}\, t_{link}^{\,m}$. The filling ratio after linkage can now be formulated as:

$$FR = \frac{k_{prec}}{V_{cav}} \left[\left(\frac{V_1 - V_0}{k_{cav}} \right)^{\frac{1}{m}} + \left(\frac{V_{cav} - V_1}{k_{cav,link}} \right)^{\frac{1}{m+\Delta m}} \right]^n \qquad (V_{cav} > V_1) \qquad (17)$$

Before linkage, FR is still described by Eq. 14. For $t > t_{link}$ the value of FR will decrease with time as the exponent for the cavity growth has increased ($\Delta m > 0$).

In Fig. 15 the evolution of the filling ratio is calculated for several cases with and without linkage. It can be seen that the two different routes for the evolution of the filling ratio shown in Fig. 10 are in good agreement with the model predictions in the absence and presence of linkage for creep cavities. It is clarified that FR can continuously increase with increasing cavity volume until the cavity is fully filled when there is no linkage. As the initial cavity volume required to induce precipitation V_0 varies, the cases without linkage form a band and cover a wide range of cavity volumes from 0.1 to 100 μm^3. However, the filling ratio decreases sharply when a linkage of creep cavities starts to occur. This hypothesis is supported by the data in Fig. 15b where the filling ratios for most of the spherical and equiaxed shaped cavities are located in the predicted filling ratio regimes assuming no pore linkage. In contrast, half of the cavities with rod, sheet and complex shapes, for which a coalescence of cavities is expected, are located in the region of a decreasing filling ratio. The remaining partially filled cavities are yet in the increasing region because they are nearly fully filled before the linkage takes place. From the present work we estimate a critical linkage volume of $V_1 \approx 200$ μm^3 at which point the filling ratio of the linked cavities starts to decrease. The observed behavior for the filling ratio of individual creep cavities is in good agreement with the predictions of this simple model.

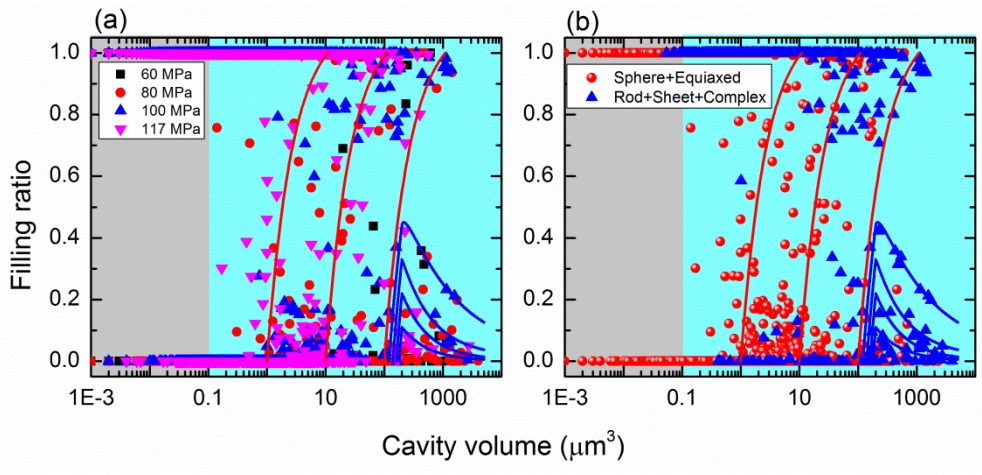

Fig. 15. The comparison between the predictions of the filling model for the cavities without (red curves) and with linkage (blue curves) and the observed filling ratios of all cavities present in the samples after creep at different loads. (a) Cavities were grouped according to different loads. (b) Cavities were grouped into two shape categories (spherical and equiaxed shaped cavities; rod, sheet and complex shaped cavities). The solid red curves based on a non-linkage model are displayed for model

parameters $n = m = 0.8$, $k_{prec}/k_{cav} = 1.1$ and $V_0 = 1$, 10 and 100 μm^3. The solid blue curves are displayed for the linkage model using the following parameter values $n = m = 0.8$, $m+\Delta m = 1.3$, $k_{prec}/k_{cav} = 1.1$, $V_1 = 200$ μm^3 and $V_0 = 120$, 140, 160 and 180 μm^3 (with $k_{cav,link}/k_{cav} = 0.01$, 0.1, 1, and 10 h$^{-0.5}$, respectively). Note that in the grey shaded region it is experimentally not possible to determine partial filling.

5. Conclusions

Synchrotron X-ray phase nano-tomography experiments were carried out successfully on creep-failed Fe-Au alloy samples after creep at 550 ^{o}C for several constant loads. 3D images of the microstructure of the Fe-Au alloy samples at nanometer length scale were obtained and analyzed. Different stages in the filling process of individual creep cavities by gold precipitation were identified to characterize the self-healing mechanism in creep-resistant steels. The following conclusions can be drawn from this study:

1) The creep cavities are predominately formed at stress-affected grain boundaries. The precipitates nucleate exclusively on grain faces and preferentially on the free cavity surface formed on these grain faces.
2) By classifying the precipitates and cavities into spherical, equiaxed, rod, sheet and complex shaped objects, it is possible to clarify their nucleation, growth and coalescence in a qualitative way. The spheres denote the smallest volume objects and reveal the nucleation sites. The equiaxed objects mainly reflect the early growth stage before coalescence, while the rod, sheet and complex objects are considered to be formed in the later growth stage and potentially influenced by coalescence.
3) The quantitative analysis of the size, shape and spatial distribution for the creep cavities and the precipitates demonstrates strong correlation between the morphology of the cavities and precipitates. It is demonstrated that the gold precipitates form preferentially at cavity surfaces and act as healing agents rather than cavitation sites for creep cavities. The self-healing character of added Au in Fe-based alloys is fully supported by this study.
4) The creep cavities develop in a coupled diffusion (both surface diffusion and grain boundary diffusion) and creep flow mode. It is derived that the shape of the cavity shows a transition from the quasi-equilibrium shape to the crack-like shape for a cavity radius in the range of $0.48 < r < 0.90$ μm as the cavity proceeds to grow. Elongated cavities at inclined grain boundaries are probably generated by grain-boundary sliding.
5) Two different time evolutions for the filling ratio of individual creep cavities are observed from the tomography results. This observation can be explained by a simple model considering the absence and presence of linkage for neighboring creep cavities. The filling ratio increases continuously for increasing cavity volumes until complete filling is achieved when there is no linkage of cavities. In contrast, the filling ratio decreases sharply once linkage between creep cavities becomes the main microstructural evolution mode.

Acknowledgements

This research is financially supported by the innovation-oriented research program (IOP) on self-healing materials of the Dutch Ministry of Economic Affairs, Agriculture and Innovation (Project SHM01017 and SHM012011) and a grant from the China Scholarship Council (CSC). The authors thank Lu Shen for her help during the synchrotron experiment. We thank Wim Verwaal and Joost van Meel at the Faculty of Civil Engineering and Geosciences, Delft University of Technology for providing the image analysis environment. We acknowledge the European Synchrotron Radiation Facility for provision of synchrotron radiation facilities and thank the beamline staff for assistance in using beamline ID16A-NI.

References

[1] J. Lemaitre, R. Desmorat, Engineering damage mechanics: ductile, creep, fatigue and brittle failures, Springer-Verlag Berlin 2005.

[2] M.F. Ashby, C. Gandhi, D.M.R. Taplin, Overview No. 3: Fracture-mechanism maps and their construction for fcc metals and alloys, Acta Metall. 27 (1979) 699-729.

[3] M. Taneike, F. Abe, K. Sawada, Creep-strengthening of steel at high temperatures using nano-sized carbonitride dispersions, Nature 424 (2003) 294-296.

[4] P.J. Ennis, A. Zielinska-Lipiec, O. Wachter, A. Czyrska-Filemonowicz, Microstructural stability and creep rupture strength of the martensitic steel P92 for advanced power plant, Acta Mater. 45 (1997) 4901-4907.

[5] K. Maruyama, K. Sawada, J. Koike, Strengthening mechanisms of creep resistant tempered martensitic steel, ISIJ Int. 41 (2001) 641-653.

[6] A. Aghajani, C. Somsen, G. Eggeler, On the effect of long-term creep on the microstructure of a 12% chromium tempered martensite ferritic steel, Acta Mater. 57 (2009) 5093-5106.

[7] S.R. White, N.R. Sottos, P.H. Geubelle, J.S. Moore, M.R. Kessler, S.R. Sriram, E.N. Brown, S. Viswanathan, Autonomic healing of polymer composites, Nature 409 (2001) 794-797.

[8] M.D. Hager, P. Greil, C. Leyens, S. van der Zwaag, U.S. Schubert, Self-Healing Materials, Adv. Mater. 22 (2010) 5424-5430.

[9] G.Q. Xu, M.J. Demkowicz, Healing of nanocracks by disclinations, Phys. Rev. Lett. 111 (2013) 145501.

[10] S. van der Zwaag, E. Brinkman, eds., Self healing materials: pioneering research in the Netherlands, IOS Press Amsterdam 2015.

[11] K. Laha, J. Kyono, S. Kishimoto, N. Shinya, Beneficial effect of B segregation on creep cavitation in a type 347 austenitic stainless steel, Scr. Mater. 52 (2005) 675-678.

[12] K. Laha, J. Kyono, N. Shinya, An advanced creep cavitation resistance Cu-containing 18Cr–12Ni–Nb austenitic stainless steel, Scr. Mater. 56 (2007) 915-918.

[13] K. Laha, J. Kyono, T. Sasaki, N. Shinya, Improved creep strength and creep ductility of type 347 austenitic stainless steel through the self-healing effect of boron for creep cavitation, Metall. Mater. Trans. A 36 (2005) 399-409.

[14] S.M. He, N.H. van Dijk, M. Paladugu, H. Schut, J. Kohlbrecher, F.D. Tichelaar, S. van der Zwaag, In situ determination of aging precipitation in deformed Fe-Cu and Fe-Cu-BN alloys by time-resolved small-angle neutron scattering, Phys. Rev. B 82 (2010) 174111.

[15] S.M. He, N.H. van Dijk, H. Schut, E.R. Peekstok, S. van der Zwaag, Thermally activated precipitation at deformation-induced defects in Fe-Cu and Fe-Cu-B-N alloys studied by positron annihilation spectroscopy, Phys. Rev. B 81 (2010) 094103.

[16] S. Zhang, G. Langelaan, J.C. Brouwer, W.G. Sloof, E. Brück, S. van der Zwaag, N.H. van Dijk, Preferential Au precipitation at deformation-induced defects in Fe–Au and Fe–Au–B–N alloys, J. Alloy. Compd. 584 (2014) 425-429.
[17] S. Zhang, J. Kohlbrecher, F.D. Tichelaar, G. Langelaan, E. Brück, S. van der Zwaag, N.H. van Dijk, Defect-induced Au precipitation in Fe–Au and Fe–Au–B–N alloys studied by in situ small-angle neutron scattering, Acta Mater. 61 (2013) 7009-7019.
[18] S. Zhang, C. Kwakernaak, W.G. Sloof, E. Brück, S. van der Zwaag, N.H. van Dijk, Self-healing of creep damage by gold precipitation in iron alloys, Adv. Eng. Mater. 17 (2015) 598-603.
[19] S. Zhang, C. Kwakernaak, F.D. Tichelaar, W.G. Sloof, M. Kuzmina, M. Herbig, D. Raabe, E. Brück, S. van der Zwaag, N.H. van Dijk, Autonomous repair mechanism of creep damage in Fe-Au and Fe-Au-B-N alloys, Metall. Mater. Trans. A 46 (2015) 5656-5670.
[20] A. Pyzalla, B. Camin, T. Buslaps, M. Di Michiel, H. Kaminski, A. Kottar, A. Pernack, W. Reimers, Simultaneous tomography and diffraction analysis of creep damage, Science 308 (2005) 92-95.
[21] E. Maire, P.J. Withers, Quantitative X-ray tomography, Int. Mater. Rev. 59 (2014) 1-43.
[22] E. Nizery, H. Proudhon, J.Y. Buffiere, P. Cloetens, T.F. Morgeneyer, S. Forest, Three-dimensional characterization of fatigue-relevant intermetallic particles in high-strength aluminium alloys using synchrotron X-ray nanotomography, Philos. Mag. 95 (2015) 2731-2746.
[23] H. Toda, S. Yamamoto, M. Kobayashi, K. Uesugi, H. Zhang, Direct measurement procedure for three-dimensional local crack driving force using synchrotron X-ray microtomography, Acta Mater. 56 (2008) 6027-6039.
[24] D. Kurumlu, E.J. Payton, M.L. Young, M. Schöbel, G. Requena, G. Eggeler, High-temperature strength and damage evolution in short fiber reinforced aluminum alloys studied by miniature creep testing and synchrotron microtomography, Acta Mater. 60 (2012) 67-78.
[25] E. Maire, O. Bouaziz, M. Di Michiel, C. Verdu, Initiation and growth of damage in a dual-phase steel observed by X-ray microtomography, Acta Mater. 56 (2008) 4954-4964.
[26] C. Landron, E. Maire, J. Adrien, H. Suhonen, P. Cloetens, O. Bouaziz, Non-destructive 3-D reconstruction of the martensitic phase in a dual-phase steel using synchrotron holotomography, Scr. Mater. 66 (2012) 1077-1080.
[27] A. Pacureanu, Y. Yang, J.C. da Silva, R. Baker, R. Barrett, S. Bohic, Y. Dabin, F. Fus, E. Gagliardini, C. Guilloud, O. Hignette, M. Hubert, M. Langer, J. Meyer, C. Morawe, J. Morse, R. Tachoueres, P. van der Linden, F. Villar, L. Weber, P. Cloetens, The ESRF Upgrade nanoprobe beamline ID16A-NI for hard X-ray coherent imaging and fluorescence microscopy, manuscript under preparation for J. Synchrotron Radiation.
[28] P. Cloetens, W. Ludwig, J. Baruchel, D. van Dyck, J. van Landuyt, J.P. Guigay, M. Schlenker, Holotomography: Quantitative phase tomography with micrometer

resolution using hard synchrotron radiation x rays, Appl. Phys. Lett. 75 (1999) 2912-2914.
[29] A. Mirone, E. Brun, E. Gouillart, P. Tafforeau, J. Kieffer, The PyHST2 hybrid distributed code for high speed tomographic reconstruction with iterative reconstruction and a priori knowledge capabilities, Nucl. Instrum. Meth. B 324 (2014) 41-48.
[30] http://www.diplib.org/.
[31] H.J. Catrakis, P.E. Dimotakis, Shape complexity in turbulence, Phys. Rev. let. 80 (1998) 968.
[32] H. Wadell, Volume, shape, and roundness of quartz particles, J. Geol. 43 (1935) 250-280.
[33] A. Borbély, F.F. Csikor, S. Zabler, P. Cloetens, H. Biermann, Three-dimensional characterization of the microstructure of a metal–matrix composite by holotomography, Mater. Sci. Eng. A 367 (2004) 40-50.
[34] A. Isaac, F. Sket, W. Reimers, B. Camin, G. Sauthoff, A.R. Pyzalla, In situ 3D quantification of the evolution of creep cavity size, shape, and spatial orientation using synchrotron X-ray tomography, Mater. Sci. Eng. A 478 (2008) 108-118.
[35] O.D. Sherby, Factors affecting the high temperature strength of polycrystalline solids, Acta Metall. 10 (1962) 135-147.
[36] J. Cadek, Creep in metallic materials, Elsevier Science Publishers B.V. Amsterdam 1988.
[37] R. Raj, M.F. Ashby, Intergranular fracture at elevated temperature, Acta Metall. 23 (1975) 653-666.
[38] A. Needleman, J.R. Rice, Plastic creep flow effects in the diffusive cavitation of grain boundaries, Acta Metall. 28 (1980) 1315-1332.
[39] T.J. Chuang, K.I. Kagawa, J.R. Rice, L.B. Sills, Overview no. 2: Non-equilibrium models for diffusive cavitation of grain interfaces, Acta Metall. 27 (1979) 265-284.
[40] I.W. Chen, Cavity growth on a sliding grain boundary, Metall. Trans. A 14 (1983) 2289-2293.
[41] G.H. Edward, M.F. Ashby, Intergranular fracture during power-law creep, Acta Metall. 27 (1979) 1505-1518.
[42] M.E. Kassner, T.A. Hayes, Creep cavitation in metals, Int. J. Plasticity 19 (2003) 1715-1748.
[43] M. Vöse, B. Fedelich, J. Owen, A simplified model for creep induced grain boundary cavitation validated by multiple cavity growth simulations, Comp. Mater. Sci. 58 (2012) 201-213.
[44] T. Shrestha, M. Basirat, I. Charit, G.P. Potirniche, K.K. Rink, Creep rupture behavior of Grade 91 steel, Mater. Sci. Eng. A 565 (2013) 382-391.
[45] A. Das, N. Roy, A.K. Ray, Stress induced creep cavity, Mater. Sci. Eng. A 598 (2014) 28-33.
[46] J.C. Fisher, Calculation of diffusion penetration curves for surface and grain boundary diffusion, J. Appl. Phys. 22 (1951) 74-77.

[47] I.W. Chen, A.S. Argon, Diffusive growth of grain-boundary cavities, Acta Metall. 29 (1981) 1759-1768.
[48] H.B. Aaron, H.I. Aaronson, Growth of grain boundary precipitates in Al-4% Cu by interfacial diffusion, Acta Metall. 16 (1968) 789-798.
[49] W.D. Nix, K.S. Yu, J.S. Wang, The effects of segregation on the kinetics of intergranular cavity growth under creep conditions, Metall. Trans. A 14 (1983) 563-570.